© 2021. Published by The Company of Biologists Ltd | Journal of Cell Science (2021) 134, jcs258340. doi:10.1242/jcs.258340

RESEARCH ARTICLE

Integrity of the short arm of the nuclear pore Y-complex is required for mouse embryonic stem cell growth and differentiation

Alba Gonzalez-Estevez[1,2,*,‡], Annalisa Verrico[1,‡], Clarisse Orniacki[1,2], Bernardo Reina-San-Martin[3,4,5,6] and Valérie Doye[1,2,§]

ABSTRACT

Many cellular processes, ranging from cell division to differentiation, are controlled by nuclear pore complexes (NPCs). However, studying the contributions of individual NPC subunits to these processes in vertebrates has long been impeded by their complexity and the lack of efficient genetic tools. Here, we use genome editing in mouse embryonic stem cells (mESCs) to characterize the role of NPC structural components, focusing on the short arm of the Y-complex that comprises Nup85, Seh1 and Nup43. We show that Seh1 and Nup43, although dispensable in pluripotent mESCs, are required for their normal cell growth rates, their viability upon differentiation and for the maintenance of proper NPC density. mESCs with an N-terminally truncated Nup85 mutation (in which interaction with Seh1 is greatly impaired) feature a similar reduction of NPC density. However, their proliferation and differentiation are unaltered, indicating that it is the integrity of the Y-complex, rather than the number of NPCs, that is critical to ensure these processes.

KEY WORDS: Nucleoporin, Seh1, Nup43, Nup85, Mios, Mouse embryonic stem cells

INTRODUCTION

Nuclear pore complexes (NPCs) are huge structures embedded in the nuclear envelope. They provide the sole gateways for bidirectional nucleocytoplasmic transport, but also participate in a wide variety of other cellular processes, including cell division and gene regulation (reviewed by Buchwalter et al., 2019; Hezwani and Fahrenkrog, 2017). NPCs are composed of ∼30 distinct proteins (called nucleoporins or Nups), each present in multiple copies and forming a ring with an eightfold rotational symmetry. Among them, structural Nups assemble to form a scaffold that anchors Nups with unfolded domains, cytoplasmic filaments and the nuclear basket (reviewed by Hampoelz et al., 2019; Lin and Hoelz, 2019).

The three-dimensional organization of the NPC scaffold has been determined at atomic resolution (reviewed by Hampoelz et al., 2019; Lin and Hoelz, 2019). It is formed by an inner rim sandwiched by two outer (cytoplasmic and nuclear) rims, the main component of which is the evolutionarily conserved Y-complex. In metazoans, this complex (also named Nup107-160 complex) comprises Nup133, Nup107, Nup96 and Sec13 (forming the stem of the Y); Nup160, Nup37 and Elys (building the long arm); and Nup85, Seh1 (also named Seh1l) and Nup43 (forming the short arm) (Fig. 1A) (Loiodice et al., 2004; Rasala et al., 2006; von Appen et al., 2015).

Functional studies in vertebrates have shown that the Y-complex is critical for NPC assembly, both after mitosis and during interphase (Doucet et al., 2010; Harel et al., 2003; Walther et al., 2003). Studies in mammalian cells also showed that in mitosis a fraction of the Y-complex localizes at kinetochores (Loiodice et al., 2004; Rasala et al., 2006), where it is required for proper chromosome congression and segregation (Platani et al., 2009; Zuccolo et al., 2007). Because the members of the Y-complex (Y-Nups) are tightly associated throughout the cell cycle (Loiodice et al., 2004; Rabut et al., 2004), they were long anticipated to work as an entity. However, one of its components, Sec13, is also part of the COPII coat complex involved in vesicle budding (Salama et al., 1993). In addition, Sec13 and Seh1 also belong to the unrelated GATOR2 complex, an indirect regulator of the mTORC1 pathway that controls cell growth and proliferation (Bar-Peled et al., 2013), further complicating the study of their function in the context of the Y-complex.

In mice, inactivation of most Y-Nups genes (namely *Elys*, *Nup96*, *Nup133*, *Nup85*, *Sec13* and *Seh1*, but not *Nup37*) lead to embryonic lethality (Faria et al., 2006; Liu et al., 2019; Lupu et al., 2008; Moreira et al., 2015; Okita et al., 2004; Terashima et al., 2020; www.mousephenotype.org/data/genes/MGI:1919964). In particular, Nup133 was found to be essential for mouse development beyond gastrulation (Lupu et al., 2008). Studies performed in mouse embryonic stem cells (mESCs) showed that Nup133 is dispensable for cell growth at the pluripotent stage, but is required for mESC differentiation (Lupu et al., 2008). In mESCs, Nup133 is dispensable for NPC scaffold assembly but required for the proper assembly of the nuclear pore basket (Souquet et al., 2018). However, it is not clear if the role of Nup133 in NPC basket assembly underlies its functions in cell differentiation.

More recently, Seh1, which is critical for proper mitotic progression in cancer cell lines (Platani et al., 2018; Platani et al., 2009; Zuccolo et al., 2007), was found to be required for the differentiation of oligodendrocyte progenitors (Liu et al., 2019). However, the potential contribution of Seh1 to cell cycle progression in non-transformed cells and at other stages of cell differentiation needed to be addressed.

Here, we assessed the requirements for Seh1 in pluripotent mESCs and upon their differentiation towards neuroectodermal lineage, determined whether these requirements reflect its role in the GATOR2-complex or in the short arm of the Y-complex, and

[1]Université de Paris, Centre National de la Recherche Scientifique, Institut Jacques Monod, F-75006 Paris, France. [2]Ecole Doctorale BioSPC, Université de Paris, Paris, France. [3]Institut de Génétique et de Biologie Moléculaire et Cellulaire, Illkirch 67404, France. [4]Inserm U 1258, Illkirch 67404, France. [5] Centre National de la Recherche Scientifique UMR (Unité Mixte de Recherche) 7104, Illkirch 67404, France. [6]Université de Strasbourg, Illkirch 67404, France.
*Present address: MRC Human Genetics Unit, Institute of Genetics and Cancer, University of Edinburgh, Edinburgh EH4 2XU, UK.
‡These authors contributed equally to this work.

§Author for correspondence (valerie.doye@ijm.fr)

A.G.-E., 0000-0002-2978-6209; A.V., 0000-0002-1458-2545; C.O., 0000-0002-2585-3179; B.R.-S.-M., 0000-0003-2083-6166; V.D., 0000-0002-7515-4931

Handling Editor: Maria Carmo-Fonseca
Received 21 December 2020; Accepted 19 April 2021

Journal of Cell Science (2021) 134, jcs258340. doi:10.1242/jcs.258340

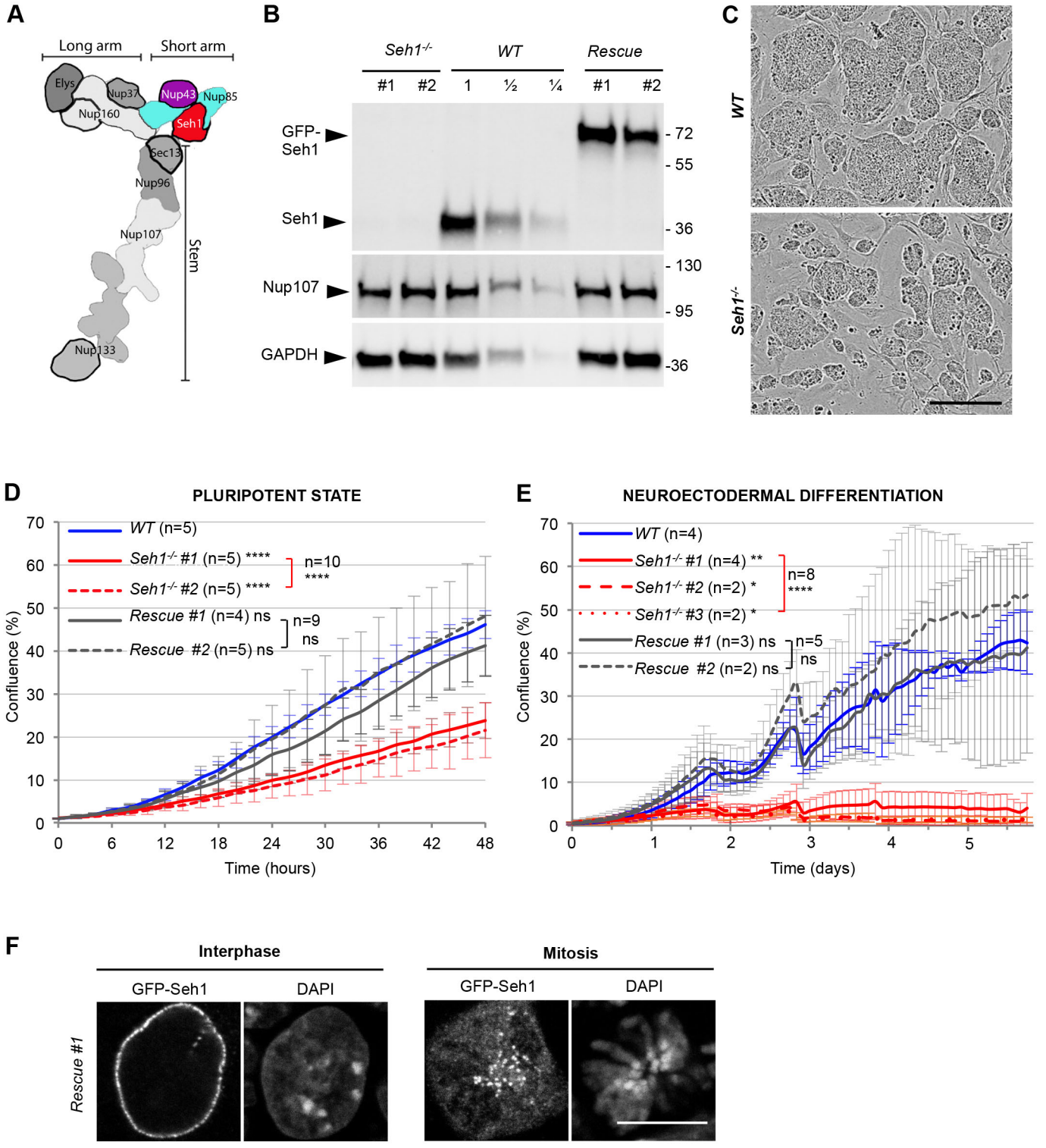

Fig. 1. Seh1 depletion leads to cell growth delay and impaired cell survival upon differentiation. (A) Schematic representation of the Y-complex (adapted from von Appen et al., 2015), highlighting the components of the short arm, namely Nup43 (shown in purple), Nup85 (blue) and Seh1 (red). β-propellers are outlined in black. (B) Western blot showing the expression of endogenous or GFP-tagged Seh1, Nup107 and GAPDH (used as loading control) in whole cell extracts from the indicated cell lines. Two- and four-fold dilutions (1/2, 1/4, respectively) of the wild-type (*WT*) extract were also loaded. Molecular weights are indicated (kDa). (C) Representative phase contrast images of wild-type and *Seh1*$^{-/-}$ (#1) mESCs colonies acquired after 2 days of growth on the IncuCyte imager. (D,E). Confluence of wild-type (blue), *Seh1*$^{-/-}$ (#1 and #2, red) and *Rescue* (#1 and #2, grey) mESCs was quantified using the IncuCyte system, either at the pluripotent stage (D) or upon differentiation towards neuroectodermal lineage (E). Data are mean±s.d. arising from the indicated number of independent experiments (*n*). Statistical analyses of these confluence curves were performed at the last time points. Brackets indicate statistics performed using all values from cell lines bearing a given mutation, compared to wild type (see Materials and Methods). **P*<0.05; ***P*<0.01; *****P*<0.0001, ns, not significant (paired two-tailed Student's *t*-test). (F) Representative spinning disk images of *Rescue* (#1) mESCs showing proper localization of GFP-Seh1 at the nuclear envelope in interphase (one plane) and at kinetochores in mitosis (a projection of three optical sections is presented). Scale bars: 300 µm (C); 10 µm (F).

Journal of Cell Science (2021) 134, jcs258340. doi:10.1242/jcs.258340

further addressed the specific function of these proteins in NPC integrity. This systematic analysis enabled us to disentangle the processes underlying the contribution of these Y-Nups in NPC assembly, nuclear size, cell growth and differentiation.

RESULTS

Seh1 is required for mESC growth and survival upon differentiation

Using CRISPR/Cas9 gene-editing technology, we obtained several independent *Seh1*$^{-/-}$ mESC clones (of which three were further examined in this study; see Materials and Methods and Table S2) (Fig. 1B). This indicates that Seh1 is dispensable for mESC viability at the pluripotent stage. However, we noticed that *Seh1*$^{-/-}$ mESCs formed smaller colonies than wild-type mESCs (Fig. 1C). Consistently, automated cell growth analyses of *Seh1*$^{-/-}$ mESCs showed a clear reduction of cell confluence compared to wild type (Fig. 1D). More strikingly, *Seh1*$^{-/-}$ cells showed a strong impairment in viability from the very early stages of monolayer differentiation towards neuroectodermal lineage, and almost no cells were recovered after 5 days (Fig. 1E; Movies 1,2).

To verify the specificity of these phenotypes, we next integrated at the permissive *Tigre* locus (Tightly regulated; Zeng et al., 2008) of *Seh1*$^{-/-}$ mESCs a GFP-tagged *Seh1* cDNA expressed under the control of the pCAG promoter. The resulting cell lines (subsequently named '*Rescue*' #1 and #2) expressed GFP-Seh1 at a level comparable to that of the endogenous untagged protein (Fig. 1B). We observed a specific enrichment of GFP-Seh1 at nuclear pores in interphase and at kinetochores throughout mitosis (Fig. 1F). Most importantly, the growth rate of the *Rescue* cell lines was comparable to that of wild-type cells both at the pluripotent stage (Fig. 1D) and upon neuroectodermal differentiation (Fig. 1E; Movie 3).

To exclude the possibility that phenotypes observed in *Seh1*$^{-/-}$ mESCs at the pluripotent stage could be due to cell adaptation, we also generated cell lines in which endogenous *Seh1* was N-terminally tagged with the 7 kDa mini auxin inducible degron (mAID) sequence to induce its acute degradation upon auxin addition (Natsume et al., 2016). A GFP tag was also introduced to allow visualization of both the localization and degradation of the resulting GFP-mAID-Seh1 fusion. Upon addition of auxin to *GFP-mAID-Seh1* mESCs, the GFP signal rapidly declined in mitotic cells, whereas, as also previously observed in HCT116 cells (Platani et al., 2018), the decay was more progressive in interphasic cells (Fig. S1A-D). Although the *GFP-mAID-Seh1* clones showed normal cell growth and differentiation properties in control conditions, the addition of auxin recapitulated both the cell growth and differentiation defects observed in *Seh1*$^{-/-}$ mESCs (Fig. S1E,F). Together, these data reveal that the lack of Seh1 specifically causes impaired cell growth of mESCs at the pluripotent stage and drastically reduced viability upon induction of neuroectodermal differentiation.

The altered growth rate of pluripotent *Seh1*$^{-/-}$ mESCs is mainly caused by extended interphases

Seh1 is known to play a role in mitosis in cancer cell lines, in which its depletion causes a delay in mitotic progression associated with chromosome congression and segregation defects (Platani et al., 2018, 2009; Zuccolo et al., 2007). Whether these defects are caused by the mislocalization of the entire Y-complex from kinetochores, as observed in HeLa cells (Platani et al., 2009; Zuccolo et al., 2007), or by the removal of Seh1 alone, has recently been questioned (Platani et al., 2018). To study the mitotic role of Seh1 in mESCs, wild-type and *Seh1*$^{-/-}$ cells were transfected with GFP-H2B and imaged for 4-6 h. Quantification of progression time from prometaphase to anaphase onset showed a ∼10 min delay in *Seh1*$^{-/-}$ compared to wild-type mESCs (from 23.7±10.1 min in wild-type to 32.8±14.5 min in Seh1$^{-/-}$ cells; mean±s.d.) (Fig. S2A). This delay is clearly milder than the one initially reported upon RNAi-induced depletion of Seh1 in HeLa cells (∼45 to 60 min; Platani et al., 2009; Zuccolo et al., 2007) but comparable to the delay recently measured upon conditionally induced degradation of Seh1 in a HCT116-derived cell line (∼12 min; Platani et al., 2018). In *Seh1*$^{-/-}$ or auxin-treated *GFP-mAID-Seh1* mitotic mESCs, the Y-complex (visualized by Nup133 and Nup85) was still properly localized at kinetochores despite the complete lack of Seh1 (Fig. S1C, Fig. S2B,C). This indicates that the mitotic delay observed in Seh1-deficient mESCs is not merely caused by the mislocalization of the Y-complex from kinetochores.

However, the 10-min prolongation of mitosis was unlikely to explain the cell growth defect of *Seh1*$^{-/-}$ mESCs (Fig. 1C,D). Therefore, we also measured the length of interphase by imaging mCherry-H2B-expressing mESCs during 24-30 h. Quantification of progression time from the end of one mitosis (set at anaphase onset) to the beginning of the next (set at prometaphase) showed that interphase length was significantly longer in *Seh1*$^{-/-}$ compared to wild-type mESCs (9.4±2.2 h in wild type versus 14.0±4.5 and 14.1±2.1 h in *Seh1*$^{-/-}$ #1 and #2, respectively; means±s.d.) (Fig. 2A).

To determine whether the lengthening of interphase in *Seh1*$^{-/-}$ mESCs was caused by retention in a specific phase of the cell cycle, we analyzed EdU-labelled and DAPI-stained wild-type and *Seh1*$^{-/-}$ mESCs by imaging flow cytometry (Fig. 2B; Fig. S2D). Except for a mild increase in the percentage of the mitotic fraction, this analysis revealed a comparable distribution of the G1, S and G2 phases of the cell cycle between *Seh1*$^{-/-}$ and wild-type mESCs (Fig. 2B). Therefore, the altered growth rate of *Seh1*$^{-/-}$ mESCs reflects a lengthening distributed over all phases of the cell cycle.

Lack of Seh1 leads to a decrease of both NPC density and nuclear size

The viability of *Seh1*$^{-/-}$ mESCs at the pluripotent stage and their impaired survival upon differentiation was reminiscent of the phenotype observed upon inactivation of Nup133, another member of the Y-complex (Lupu et al., 2008). Because Nup133 loss was recently demonstrated to affect NPC basket assembly (as revealed by a lack of TPR staining in about 50% of the NPCs) (Souquet et al., 2018), we decided to examine the impact of *Seh1* inactivation on NPC assembly. Therefore, we quantified the average fluorescence intensity at the nuclear envelope of TPR, Nup98 and Nup133 in wild-type and *Seh1*$^{-/-}$ mESCs using a GFP-tagged cell line for internal reference, as reported previously (Souquet et al., 2018; see Materials and Methods). This analysis revealed a mild but significant reduction (in the range of 20-35%) in the signal of these three nucleoporins in *Seh1*$^{-/-}$ relative to wild-type mESCs (Fig. 3A-C). The fact that the reduced intensity at the nuclear envelope is not restricted to TPR indicates that, unlike what was previously observed in *Nup133*$^{-/-}$ mESCs, the lack of Seh1 leads to a decrease in the total number of NPCs rather than alteration of a specific substructure. This defect in NPC density was also observed upon auxin-induced depletion of Seh1 (Fig. 3D), and was largely rescued by stable expression of GFP-Seh1 (Fig. 3A-C).

It was recently proposed that nuclear size is sensitive to NPC density and nuclear import capacity in cultured mammalian cells (Jevtić et al., 2019). The decreased NPC density observed upon

Journal of Cell Science (2021) 134, jcs258340. doi:10.1242/jcs.258340

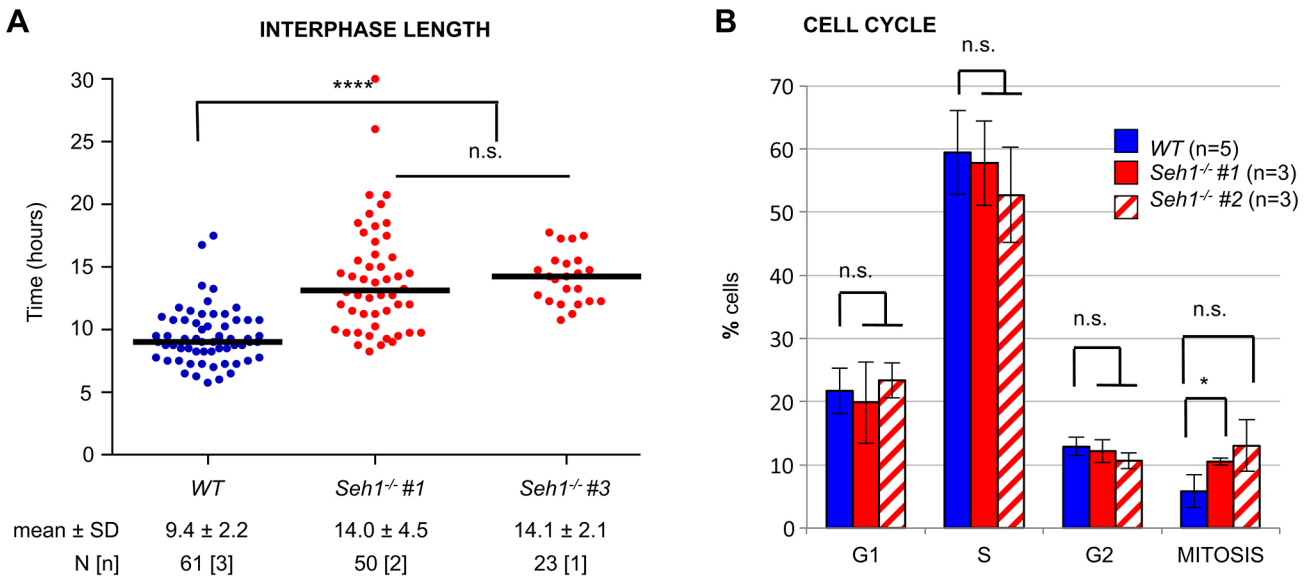

Fig. 2. The altered growth rate of *Seh1*$^{-/-}$ mESCs reflects a lengthening distributed over all phases of the cell cycle. (A) Quantification of interphase length of wild-type and *Seh1*$^{-/-}$ mESCs (two distinct clones). The black bars represent the median and each dot represents one individual cell. The mean duration of interphase, as well as the number of imaged cells (N) and experiments (*n*), is indicated. ****P<0.0001; n.s., not significant (Mann–Whitney test). (B) Cell cycle profiles of wild-type and two *Seh1*$^{-/-}$ clones generated by ImageStream using the workflow analysis presented in Fig. S2D. For each cell line, at least 3000 cells acquired in at least three distinct experiments, as indicated, were analyzed. Data are presented as the mean±s.d. *P<0.05; n.s., not significant (paired two-tailed Student's *t*-test).

Seh1 inactivation thus prompted us to measure nuclear size in these mutant mESCs. This analysis revealed a ∼10% reduction of the nuclear surface in *Seh1*$^{-/-}$ mESCs, a phenotype that was rescued by the GFP-Seh1 transgene (Fig. 4A). A significant reduction in nuclear size could also be observed in auxin-treated *GFP-mAID-Seh1* mESCs (Fig. 4B).

Seh1-deficient mESCs thus exhibit several distinct phenotypes: altered cell growth, lethality upon differentiation, reduced NPC density and nuclear size. We next aimed to determine whether these defects were linked to each other and whether they reflected functions of Seh1 as part of the Y-complex or the GATOR2 complex, or both.

Mios is not required for proper cell growth and cell differentiation in mESCs

Within the GATOR2 complex, Seh1 directly interacts with Mios (also known as Mio, missing oocyte in *Drosophila* and Sea4 in budding yeast) (Senger et al., 2011; Bar-Peled et al., 2013; Algret et al., 2014). Our western blot analyses revealed decreased protein levels of Mios in *Seh1*$^{-/-}$ compared to wild-type mESCs (Fig. 5A), a result consistent with studies in other species and cell types (Platani et al., 2018, 2015; Senger et al., 2011). To assess whether this reduction in Mios could cause the cell growth and differentiation phenotypes observed in *Seh1*$^{-/-}$ mESCs, we inactivated *Mios* in mESCs via CRISPR/Cas9 (Fig. 5A; Table S2). Immunoprecipitation experiments performed using anti-Seh1 antibodies revealed that lack of Mios prevents Seh1 interaction with Wdr24, another GATOR2 complex component (Bar-Peled et al., 2013) (Fig. 5B). This points to Mios as being the main direct partner linking Seh1 to the rest of the GATOR2 complex, a result complementing data previously obtained in budding yeast and *Drosophila* (Algret et al., 2014; Dokudovskaya and Rout, 2015; Cai et al., 2016). Analyses of independent *Mios*$^{-/-}$ clones revealed only a minor reduction of cell growth at the pluripotent stage compared to wild-type mESCs (14±15% decrease in confluence after 48 h of growth, while the reduction was 44±14% for *Seh1*$^{-/-}$ mESCs; mean±s.d.; Fig. 5C). In addition, *Mios*$^{-/-}$ cells underwent differentiation towards the neuroectodermal lineage with a comparable cell density (Fig. 5D) and morphology (A.G.-E. and V.D., unpublished) as wild-type cells. Finally, quantitative analyses did not reveal any significant alteration in either NPC density or nuclear size in *Mios*$^{-/-}$ compared to wild-type mESCs (Fig. 5E,F). Together, these experiments indicate that neither the growth and differentiation defects, nor the altered nuclear pore density and nuclear sizes observed in *Seh1*$^{-/-}$ mESCs can be merely attributed to the decreased levels of Mios.

Mutations affecting the short arm of the Y-complex impair NPC assembly, but with distinct impacts on cell proliferation and differentiation

Having excluded Mios destabilization as the main cause of the defects of *Seh1*$^{-/-}$ mESCs, we next focused our attention on the partners of Seh1 localized on the short arm of the Y-complex (Fig. 1A, Fig. 6A). We first inactivated *Nup43*, another small β-propeller-folded nucleoporin that is specific to metazoan Y-complexes (Neumann et al., 2010). We obtained viable clones upon CRISPR/Cas9-mediated *Nup43* knockout in mESCs that, however, displayed impaired proliferation at the pluripotent stage (Fig. 6B,C). Although this growth defect was milder than the one observed in pluripotent *Seh1*$^{-/-}$ mESCs, *Nup43*$^{-/-}$ nevertheless underwent drastic cell death upon neuroectodermal differentiation, comparable to that of differentiating *Seh1*$^{-/-}$ cells (Fig. 6D). *Nup43*$^{-/-}$ mESCs also displayed a reduced NPC density comparable to that observed in the various *Seh1*$^{-/-}$ mESC lines, as revealed by the reduced intensity of Nup133, Nup98 and TPR labelling at nuclear pores (Fig. 7A-C, see also Fig. 3A-C). Finally, these cells showed no significant reduction in nuclear size (Fig. 7D). Together, these data indicate that inactivation of *Nup43* mimics, albeit with a slightly milder impact, most of the phenotypes caused by *Seh1* inactivation.

To determine whether these shared phenotypes reflect a function of these Nups within the short arm of the Y-complex, we next aimed to impair Seh1 recruitment to the NPCs. Structural studies have

Journal of Cell Science (2021) 134, jcs258340. doi:10.1242/jcs.258340

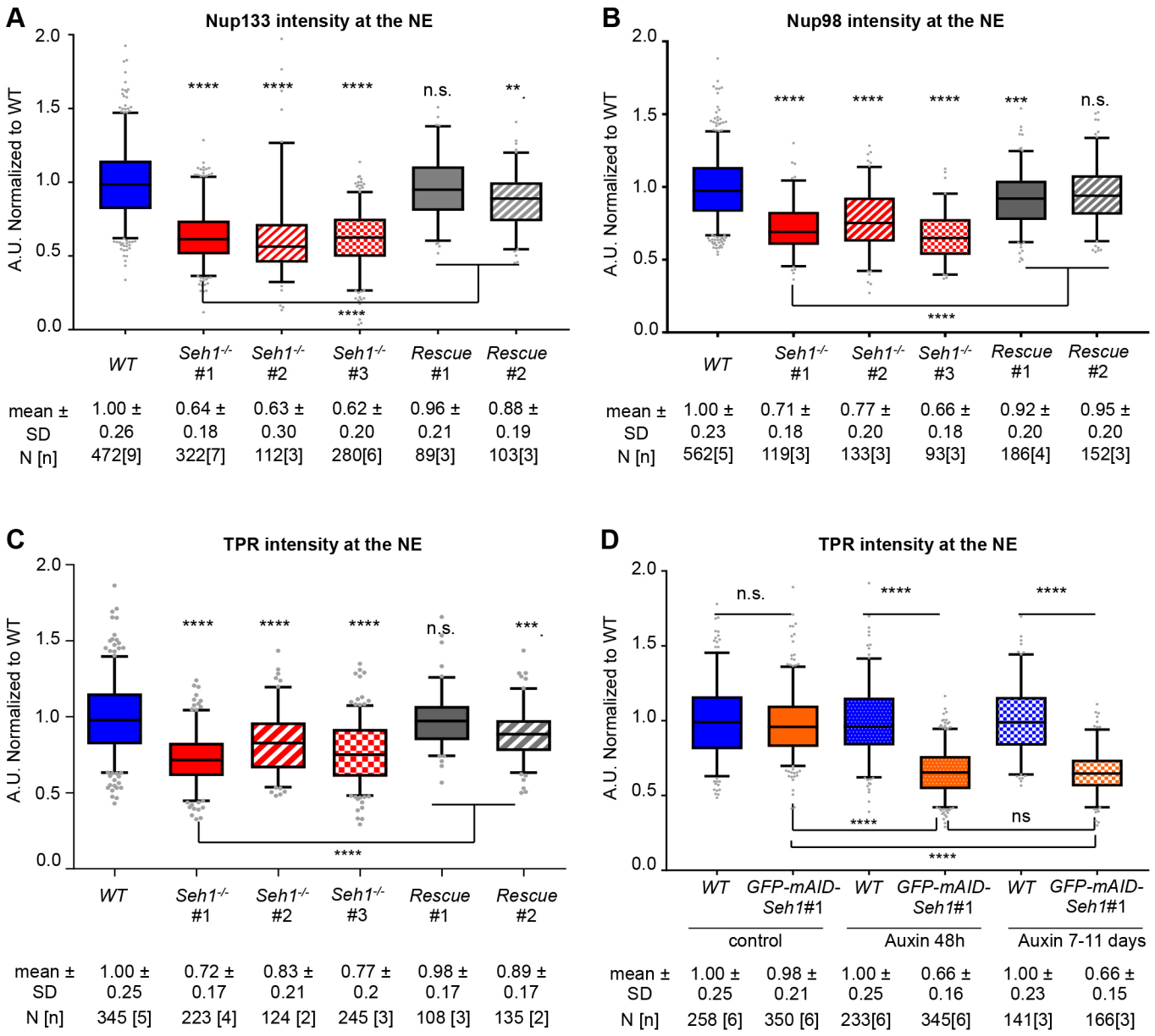

Fig. 3. Quantification of NPC density in *Seh1* mutant cell lines. Normalized signal intensities at the nuclear envelope (NE) of Nup133 (A), Nup98 (B) and TPR (C,D) were quantified and box plots were generated as described in Materials and Methods. The mean value was set at 1 for wild-type (*WT*) mESCs. For each cell line, the number of cells quantified (N), the number of distinct experiments (*n*). In D, cells were treated with ethanol (control) or auxin as indicated. ***P*<0.01; ***P<0.001; *****P*<0.0001, n.s., not significant (Mann–Whitney test). A.U., arbitrary units.

shown that budding yeast Seh1 binds to Nup85 through its N-terminal domain forming the seventh blade to complete the β-propeller structure of Seh1 (Brohawn et al., 2008; Debler et al., 2008). Homology modelling predicted that the human Nup85-Seh1 interface similarly involves β-sheets within the Nup85 N-terminal domain that complete the Seh1 β-propeller (von Appen et al., 2015; see Fig. 6A). We thus attempted to prevent Seh1 binding to Nup85 by deleting most of this blade (two β-sheets encoded by exon 2 of mouse Nup85; coloured in yellow in Fig. 6A) and inserting instead the sequence of the bulky GFP. We obtained viable mESC lines in which the resulting ΔE2-GFP-Nup85 fusion, expressed as the unique form of Nup85 in the cell (Fig. 6B; Fig. S3C), was properly localized at both NPCs and kinetochores (Fig. S3A).

To determine whether this deletion within Nup85 indeed prevented its interaction with Seh1, we performed immunoprecipitation on wild-type or *ΔE2-GFP-Nup85* mESC lysates using antibodies directed against either Nup85 itself, or Nup107, another Y-complex constituent (Fig. 1A). Mass-spectrometry analysis showed that ΔE2-GFP-Nup85 interacts with all the members of the Y-complex except Seh1 (Fig. S3B). Because none of the available Seh1 antibodies we tested properly recognized endogenous mouse Seh1 in immunofluorescence experiments, we also introduced within *GFP-Seh1* cells the same N-terminal deletion of Nup85, this time tagged with mCherry (Fig. S3C, Table S2). Although ΔE2-mCherry-Nup85 was properly localized at NPCs and kinetochores (Fig. 8A,B), GFP-Seh1 was, at most, only barely detectable at kinetochores in these cells (Fig. 8B,D; quantifications revealed 7-8±5-7% mean±s.d. residual signal in ΔE2-mCherry-Nup85- compared to wt-Nup85-expressing cells). The mislocalization of Seh1 from kinetochores is consistent with its

Journal of Cell Science (2021) 134, jcs258340. doi:10.1242/jcs.258340

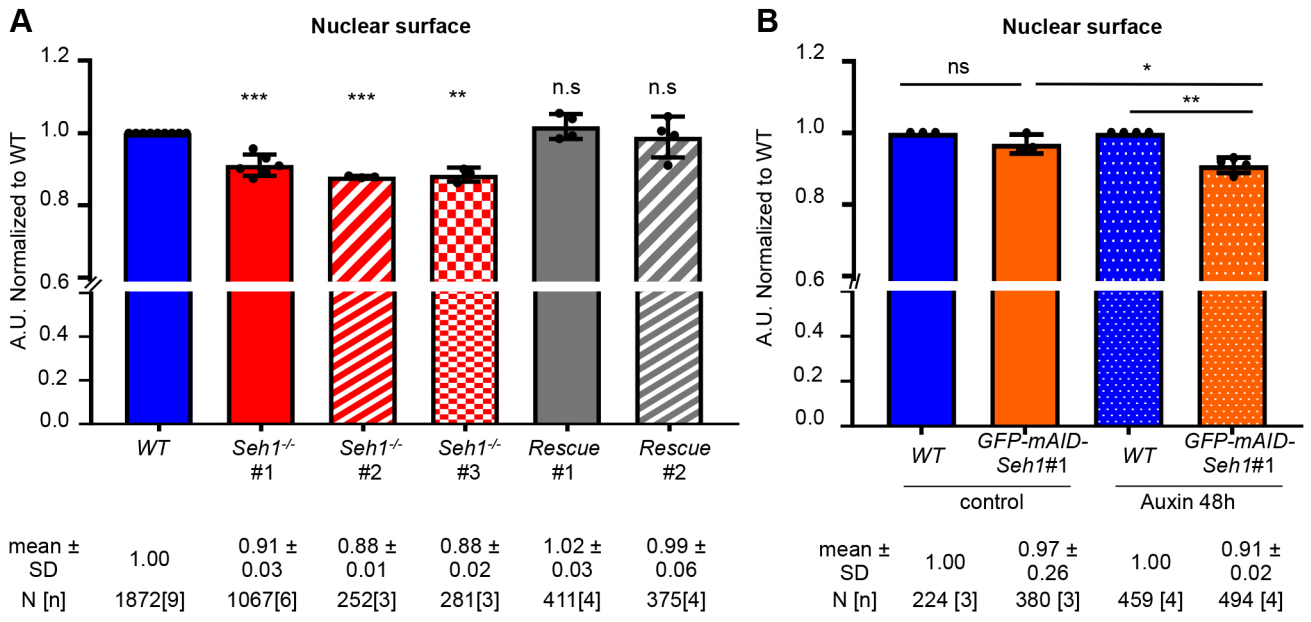

Fig. 4. Quantification of nuclear sizes in *Seh1* mutant cell lines. Quantification of nuclear surface was performed as described in Materials and Methods. The mean value was set at 1 for wild-type (*WT*) mESCs. Data are mean±s.d. of nuclear surface values from (*n*) independent experiments (displayed as dots). Unless specified by lines, samples were compared to wild type for statistical analyses (see Materials and Methods). **P*<0.05; ***P*<0.01; ***P<0.001; n.s., not significant (paired two-tailed Student's *t*-test). A.U., arbitrary units.

impaired interaction with ΔE2-GFP-Nup85 seen at the biochemical level and with previous studies, indicating that the Y-complex is recruited as an entity to kinetochores (Loiodice et al., 2004). In contrast, we could still detect some punctate GFP-Seh1 signal at the nuclear envelope (26-27% residual signal; Fig. 8A,C). The relative persistence of GFP-Seh1 at NPCs, compared to kinetochores in *ΔE2-mCherry-Nup85* cells, likely reflects the existence of additional minor binding sites for Seh1 at NPCs that either involve Nups not belonging to the Y-complex, or implies the presence of interfaces generated by the three-dimensional-organization of the Y-complex within the assembled mammalian NPC (Huang et al., 2020; Kosinski et al., 2016; von Appen et al., 2015).

Unexpectedly, analysis of cell differentiation did not reveal any significant differences between *ΔE2-GFP-Nup85* and wild-type mESCs (Fig. 6D). In addition, *ΔE2-GFP-Nup85* mESCs only displayed a minor cell growth defect in the pluripotent state (9±7% decrease in confluence after 48 h of growth compared to wild-type mESCs, whereas the reduction was 60±7% and 38±11% for *Seh1*$^{-/-}$ and *Nup43*$^{-/-}$ cells, respectively; mean±s.d.; Fig. 6C). Nevertheless, pluripotent *ΔE2-GFP-Nup85* cells displayed a significant reduction in the intensity of Nup133, Nup98 and TPR at the nuclear envelope (Fig. 7A-C). These decreased signals were comparable to those observed in *Seh1*$^{-/-}$ and *Nup43*$^{-/-}$ mESCs, and yet, as in the case of *Nup43*$^{-/-}$, they were not accompanied by a significant reduction in nuclear size (Fig. 7D). Analysis of the *ΔE2-GFP-Nup85* cell lines thus showed that perturbed recruitment of Seh1 at NPCs leads to a reduction in NPC number, but does not impact cell growth and differentiation.

DISCUSSION

This study has revealed that Seh1 and Nup43 are dispensable for mESC viability in the pluripotent state but become critical upon their differentiation. In view of the reported embryonic lethality of the *Seh1* knockout in mouse, an impaired differentiation of *Seh1*$^{-/-}$ mESCs could have been anticipated (Liu et al., 2019). In contrast, no role in development had been described previously for Nup43, which is specific to metazoans (Neumann et al., 2010). Although the requirement for differentiation was reminiscent of the phenotype observed upon inactivation of *Nup133*, we observed that Seh1 and Nup43, are, unlike Nup133 (Lupu et al., 2008), also required for the proper growth of mESCs in the pluripotent state. Importantly, this altered growth is not simply caused by a mitotic defect, as might have been assumed given the mitotic roles of Seh1 in cancer cells (Platani et al., 2018; Platani et al., 2009; Zuccolo et al., 2007), but rather reflects a lengthening of all phases of the cell cycle.

We initially anticipated that the phenotypes of *Seh1*$^{-/-}$ mESCs could be caused by a combination of its functions within the Y- and the GATOR2-complexes. However, the fact that the *Mios*$^{-/-}$ cells did not feature any NPC assembly, nuclear size or cell differentiation defects rather suggests that *Seh1*$^{-/-}$ phenotypes (except perhaps a mild contribution to cell growth rates) are unlikely to result from a combination of defects in NPC and GATOR function. Moreover, *Nup43*$^{-/-}$ mESC phenotypes are very similar to those of *Seh1*$^{-/-}$ mESCs, despite the fact that Nup43 did not interact with Mios.

Our data also showed that integrity of the short arm of the Y-complex is important for proper NPC density, further distinguishing its function from that of Nup133, which specifically affects NPC basket assembly in mESCs (Souquet et al., 2018). The observed reduction in NPC density in our *Seh1*$^{-/-}$, *Nup43*$^{-/-}$ and *ΔE2-GFP-Nup85* clones likely reflects an absolute reduction in total NPC number, as there was no corresponding increase in nuclear surface in these cells (instead, nuclear size was mildly reduced in *Seh1*$^{-/-}$ mESCs). Different mechanisms may explain the requirement for an intact short arm of the Y-complex to ensure proper NPC numbers. Considering the critical roles of the Y-complex in both NPC re-assembly after mitosis and *de novo* NPC assembly in interphase (Doucet et al., 2010; Harel et al., 2003; Walther et al., 2003), the short arm of the Y-complex might be required for the efficient recruitment of the Y-complex either to the mitotic chromatin (a

Journal of Cell Science (2021) 134, jcs258340. doi:10.1242/jcs.258340

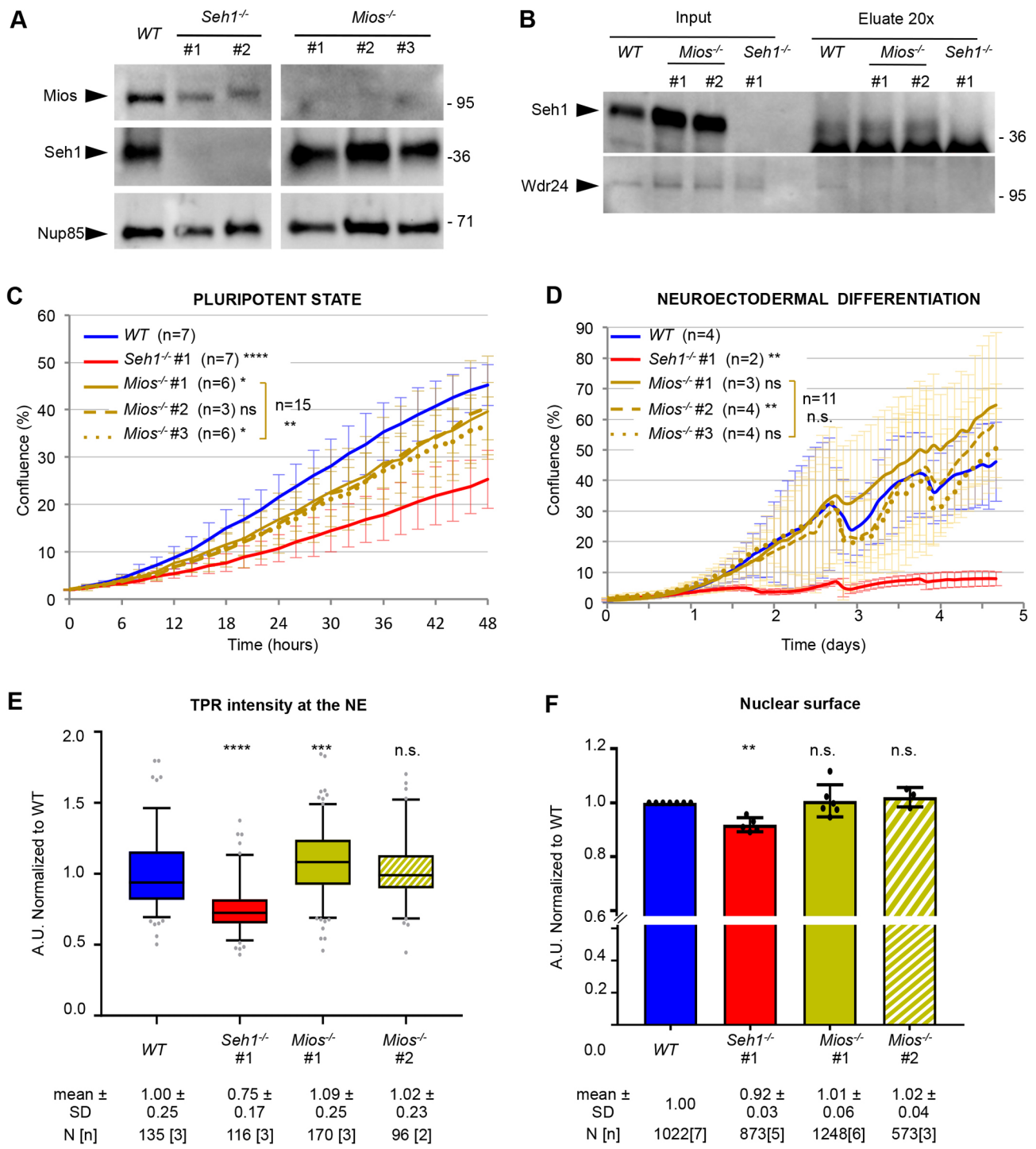

Fig. 5. *Mios*$^{-/-}$ mESCs do not mimic the growth and differentiation defects of *Seh1*$^{-/-}$ mESCs, nor their decreased NPC density and nuclear size. (A) Whole cell extracts of wild-type (*WT*), *Seh1*$^{-/-}$ (#1 and #2) and *Mios*$^{-/-}$ mESCs (three independent clones) were analyzed by western blotting, using the indicated antibodies. Molecular masses are indicated on the right (kDa). (B) Immunoprecipitation experiment using anti-Seh1 antibodies and wild-type, *Mios*$^{-/-}$ (#1 and #2), or *Seh1*$^{-/-}$ (#1) mESC protein extracts. Inputs and eluates (20× equivalent) were analyzed by western blotting, using the indicated antibodies. Molecular markers are indicated on the right (kDa). (C,D) Cell growth analyses (using percentage of confluence as proxy) were performed with the IncuCyte system for wild-type, *Seh1*$^{-/-}$ and three distinct *Mios*$^{-/-}$ clones at pluripotent state (C), and upon neuroectodermal differentiation (D). Statistical analyses were performed at the last time points. Brackets indicate statistics performed using all values from cell lines bearing a given mutation, compared to wild type (see Materials and Methods). (E,F) Quantification of TPR signal intensity at the nuclear envelope (NE) (E, presented as box plots, generated as described in Materials and Methods) and of the nuclear surface [F, graphs presenting the mean values and standard deviations from (*n*) distinct experiments, each displayed as a dot] were performed for wild-type, *Seh1*$^{-/-}$ and two *Mios*$^{-/-}$ clones as described in Materials and Methods. For each cell line, the total number of cells (N) acquired in (*n*) distinct experiments are indicated. For statistical analyses (see Materials and Methods) samples were compared to wild type. The mild (9%) increase in TPR density in *Mios*$^{-/-}$ #1 mESCs was not observed for *Mios*$^{-/-}$ #2 cells, and likely reflects a clonal-related variation not linked to the lack of Mios. The data for wild-type and *Seh1*$^{-/-}$ mESCs (used as reference strains) shown in panels C, D and F include some data from experiments already presented in Fig. 1D,E and Fig. 4A. **P*<0.05; ***P*<0.01; ***P<0.001; *****P*<0.0001; n.s., not significant (C, D and F, paired two-tailed Student's *t*-test; E, Mann–Whitney test).

Journal of Cell Science (2021) 134, jcs258340. doi:10.1242/jcs.258340

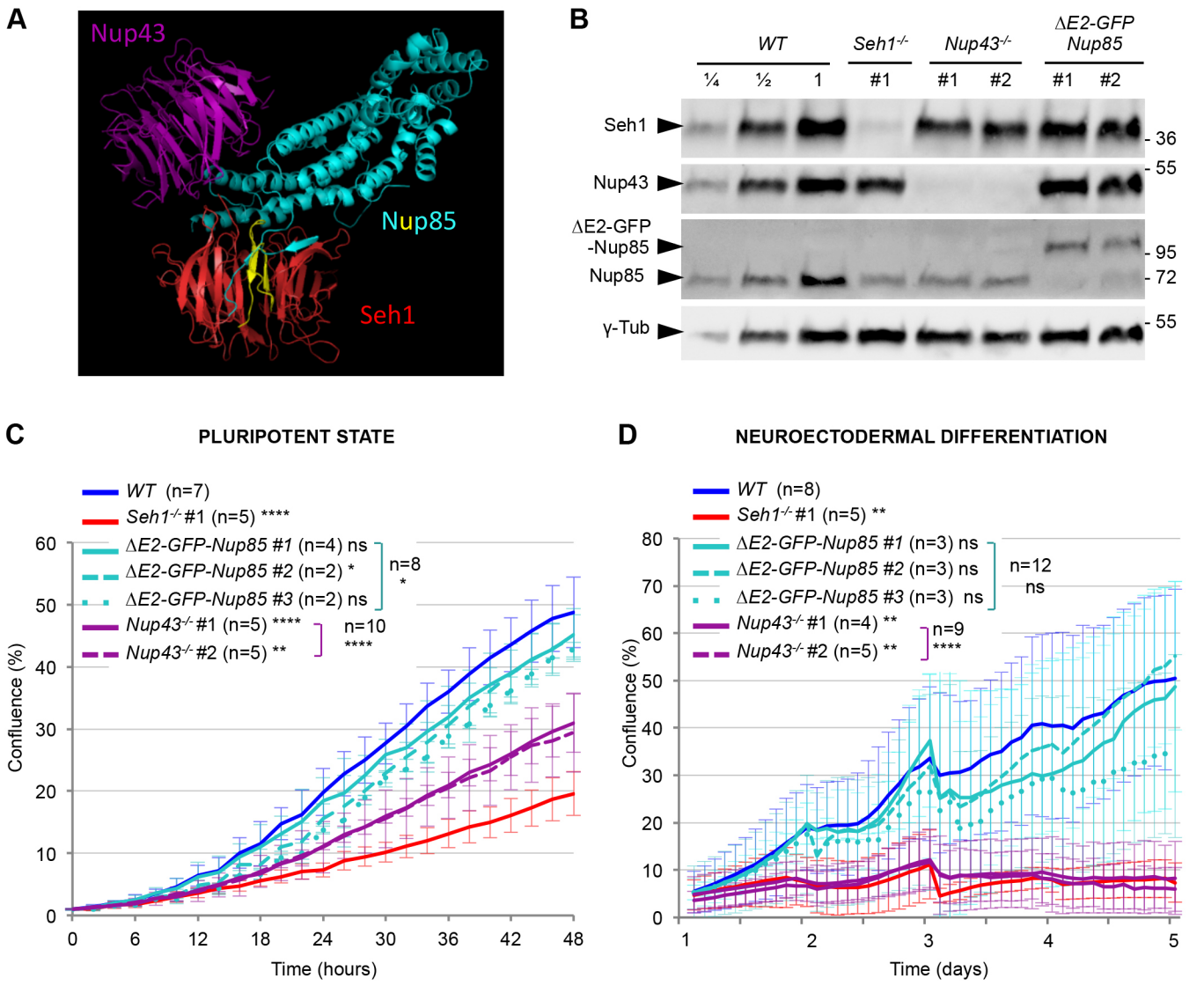

Fig. 6. Impact of Y-complex short arm mutations on mESC proliferation and differentiation. (A) Predicted model of human Nup43 (shown in purple), Nup85 (blue and yellow) and Seh1 (red) interactions (von Appen et al., 2015; PDB code: 5A9Q) visualized using Pymol. The β-sheets within the N-terminal domain of Nup85 that are deleted in the ΔE2-GFP/mCherry-Nup85 fusions are shown in yellow. (B) Whole cell extracts of the indicated cell lines were analyzed by western blot using anti-Seh1, -Nup43, -Nup85 and γ-tubulin antibodies. Two- and four-fold dilution (1/2, 1/4) of the wild-type (*WT*) mESC extract were also loaded. Molecular markers are indicated on the right (kDa). (C,D). Cell growth analyses were performed using the IncuCyte system for wild-type, *Seh1*$^{-/-}$, *ΔE2-GFP-Nup85* and *Nup43*$^{-/-}$ mESCs at pluripotent state (C) and upon neuroectodermal differentiation (D). Statistical analyses were performed at the last time-points. Brackets indicate statistics performed using all values from cell lines bearing a given mutation compared to wild type (see Materials and Methods). Data are mean±s.d. **P*<0.05; ***P*<0.01; *****P*<0.0001; ns, not significant (paired two-tailed Student's *t*-test). The data for wild type and *Seh1*$^{-/-}$ (used as reference strains) shown in panels C and D include experiments already presented in Fig. 1D,E.

hypothesis consistent with the minor reduction of Y-complex levels on chromatin reported upon Seh1 depletion in HCT116 cells – Platani et al., 2018), or to the nuclear envelope in interphase (a process involving Nup153 – Vollmer et al., 2015). Alternatively, Nup43 and Seh1 may contribute to the stabilization of the NPC scaffold by virtue of their direct interactions with neighbouring subunits from either Y-complexes or inner ring complexes (Huang et al., 2020; Kosinski et al., 2016; von Appen et al., 2015). NPCs lacking these stabilizing interactions might then be recognized by one of the recently described quality-control mechanisms that mediate the removal of some misassembled NPCs from the nuclear envelope (reviewed by Webster and Lusk, 2016).

Finally, our analysis of the *ΔE2-GFP-Nup85* cell lines indicates that the reduction in NPC density observed in *Seh1*$^{-/-}$ and *Nup43*$^{-/-}$ mESCs is not sufficient to impact cell growth and differentiation. The lack of major growth and differentiation defects in *ΔE2-GFP-Nup85* cells, in which Seh1 is largely mislocalized from NPCs, could reflect an 'off-pore' function of Seh1, or a function of Seh1 that does not require its normal stoichiometry within NPCs (for instance, a localization restricted to the cytoplasmic or nuclear side of the NPCs). At NPCs, Seh1 and Nup43 might be required for the proper recruitment and positioning of the mRNA export and remodelling machinery, an established function of the short arm of the Y-complex in budding yeast (Fernandez-Martinez et al., 2016). Alternatively, whether at pores or elsewhere in the nucleus, Seh1 and Nup43 may impact cell growth and differentiation by directly contributing to gene regulation, as now reported for a few Nups in mammalian cells (reviewed by

Journal of Cell Science (2021) 134, jcs258340. doi:10.1242/jcs.258340

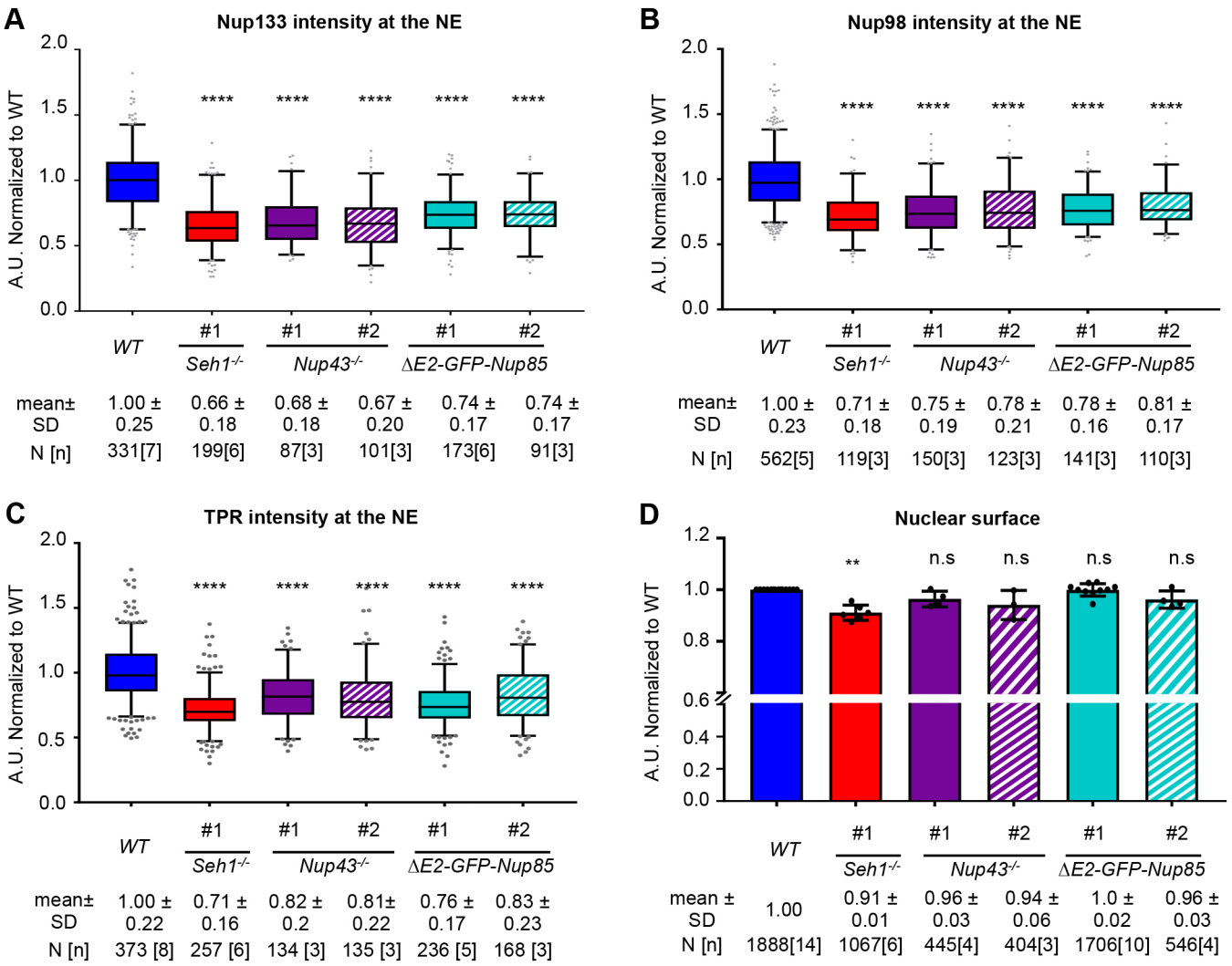

Fig. 7. Quantification of NPC density and nuclear size in Δ*E2-GFP-Nup85* and *Nup43*$^{-/-}$ mESC lines. (A-C) Normalized signal intensities at the nuclear envelope (NE) of Nup133 (A), Nup98 (B) and TPR (C) (presented as box plots, generated as described in Materials and Methods) and nuclear surfaces (D; data are presented as mean and s.d. of *n*=distinct experiments, each displayed as a dot) were quantified as described in Materials and Methods. The number of cells (N) and distinct experiments (*n*) are indicated. For statistical analyses (see Materials and Methods) samples were compared to wild type (*WT*). ***P*<0.01; *****P*<0.0001; n.s., not significant (A-C, Mann–Whitney test; D, paired two-tailed Student's *t*-test). A.U., arbitrary units. The data for wild type and *Seh1*$^{-/-}$ (used as reference strains) include experiments already presented in Figs 3 and 4.

Buchwalter et al., 2019; Pascual-Garcia and Capelson, 2019; see also Scholz et al., 2019). In particular, Seh1 was recently found to participate in oligodendrocyte differentiation, acting as a platform to recruit transcription and chromatin remodelling factors (Olig2 and Brd7) (Liu et al., 2019). We hypothesize that both Seh1 and Nup43 may specifically interact with factors required for gene regulation and chromatin organization in mESCs, hence contributing to the early stages of pluripotent cell growth and differentiation.

MATERIALS AND METHODS

The plasmids used in this study are listed in Table S1. They were either previously published or generated using standard molecular cloning techniques, including restriction digests (Fastdigest, Thermo Fisher Scientific, Waltham, MA, USA), PCR amplification using proofreading DNA polymerases (Phusion HF, New England Biolab, Ipswich, MA, USA) and In-Fusion HD Cloning Kits (Clontech, Mountain View, CA, USA) or NEBuilder HiFi DNA Assembly Cloning Kits (New England Biolabs). The *Mios* and *Nup43* gRNAs were integrated in a linear plasmid (GeneArt CRISPR Nuclease Vector – OFP-Cas9) following the manufacturer's instructions. The other Cas9 vectors (pX-280, pX-672, pX-853 and pX-864) were assembled by golden gate cloning (Engler et al., 2009). For all constructs, PCR-amplified fragments and junctions were checked by sequencing. Plasmid maps are available upon request.

Cell lines, growth conditions, transfection and CRISPR/Cas9-based genome editing

The cell lines used in this study are listed in Table S2. All cells were grown at 37°C and 5% CO_2.

DR4-mouse embryonic fibroblast (DR4-MEFs) feeder cells (Applied StemCells) were grown in Dulbecco's modified Eagle's medium (DMEM) (Gibco/Thermo Fisher Scientific) supplemented with 15% heat-inactivated foetal bovine serum (FBS, Gibco), 100 U/ml penicillin-100 µg/ml streptomycin (P/S) (Gibco) and 2 mM L-glutamine (Gibco). DR4-MEFs were inactivated using 8.5 µg/ml mitomycin-C (Sigma-Aldrich, St Louis, MO, USA) for 3 h.

HM1 (Selfridge et al., 1992) and derivative mESCs clones were grown in serum/leukemia inhibitory factor (LIF)-containing stem cell medium:

Journal of Cell Science (2021) 134, jcs258340. doi:10.1242/jcs.258340

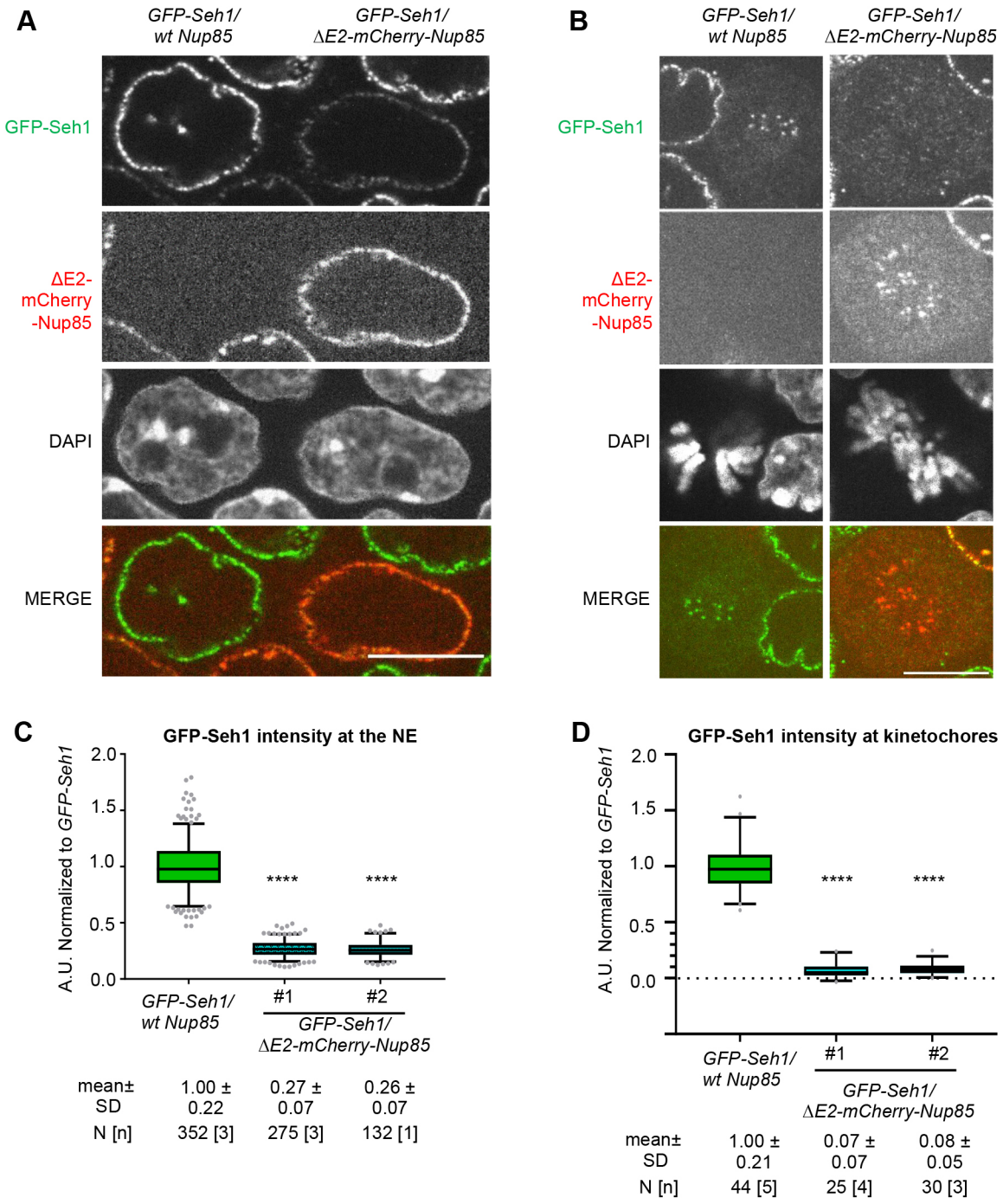

Fig. 8. Impaired GFP-Seh1 localization at NPCs and kinetochores in Δ*E2-mCherry-Nup85* mESCs. (A,B) Representative spinning disk images (single *z*-section) of interphase (A) and mitotic (B) *GFP-Seh1* cells (left) mixed with Δ*E2-mCherry-Nup85*/*GFP-Seh1* cells (right). Scale bars: 10 µm. (C,D) GFP-Seh1 intensity at the nuclear envelope (NE) (C) and at kinetochores (D) was quantified in *GFP-Seh1* and Δ*E2-mCherry-Nup85*/*GFP-Seh1* and presented as box-plots (generated as described in Materials and Methods). The number of cells (N) acquired in (*n*) independent experiments is indicated. Values were normalized for each field (C) or for each experiment (D) to the average intensity of the signal acquired for *GFP-Seh1* cells at the nuclear envelope and kinetochores, respectively. ****P<0.0001 (Mann–Whitney test). A.U., arbitrary units.

DMEM (EmbryoMax, Millipore, Burlington, MA, USA); P/S (Gibco); 2 mM L-glutamine (Gibco); 15% heat-inactivated ESC-Qualified FBS (Gibco), non-essential amino acids (Gibco); nucleosides (Millipore); β-mercaptoethanol (Gibco); and 10^3 units/ml LIF (ESGRO, Millipore). mESCs were grown on inactivated DR4-MEFs (MEF-derived feeders) plated on 0.1% gelatin (Sigma-Aldrich), and were passaged every 2 or 3 days using 0.05% Trypsin (Gibco). mESCs were used at passages below 30. Lack of contamination between the mutant cell lines was assessed by PCR on genomic DNA, proper GFP or mCherry expression when pertinent, and western blot analyses. Frequent DAPI staining ensured lack of major contamination by mycoplasm. When required, cells were counted using a Countess automated cell counter (Invitrogen, Carlsbad, CA, USA).

For transfections, mESCs were plated onto DR4-MEFs in medium without P/S. Plasmid DNA and Lipofectamine 2000 (Invitrogen) were mixed in OptiMEM (Invitrogen) and added to the cells according to the manufacturer's instructions.

For CRISPR/Cas9 editing, 5×10^5 mESCs were transfected as indicated in Table S2, with one or two plasmids (3 µg each) directing the expression of one or two gRNAs along with Cas9 (wild-type or high fidelity, HF) fused to GFP, mCherry or OFP. gRNAs were designed using the Benchling website (www.benchling.com) and are listed in Table S3. When indicated, DNA sequences of interest (PCR product 1-4 µg, or 3 µg of linearized plasmid) flanked by homology-directed repair arms were co-transfected (Fig. S4). Following selection (as detailed below), individual clones were picked, amplified and further characterized. For each clone, chromosome spreads were also performed (chromosome counts are indicated in Table S2).

To establish *Seh1*$^{-/-}$, *Mios*$^{-/-}$ and *Nup43*$^{-/-}$ cell lines, cells were collected by trypsinization 2 days after transfection, resuspended in 1 ml fluorescence-activated cell sorting (FACS) buffer (PBS plus 10% FBS, Gibco, plus P/S) and sorted based on Cas9 expression (EGFP or OFP signal). A total of 2000 FACS-sorted cells were plated in 100 mm culture dishes. Individual clones picked 6-12 days after sorting were then characterized using western blot and PCR on genomic DNA followed by sequencing (the identified Indels are listed in Table S2).

To establish the *OsTir* cell line, 200 µg/ml Geneticin (Gibco, Life Technologies 10131-019) was added to the medium 2 days after transfection. Geneticin-resistant clones (expected to have integrated the pCAG-OsTir-T2A-NeoR sequence at the *Tigre* locus) were picked after 5 days and characterized by western blot with antibodies directed against the OsTir receptor. PCR on genomic DNA was also performed to determine the number of *Tigre* alleles bearing the transgene.

To generate the Seh1 rescue (expressing GFP-Seh1 under the pCAG promoter at the *Tigre* locus), GFP-Seh1, GFP-mAID-Seh1, ΔE2-GFP-Nup85 and [ΔE2-mCherry-Nup85] cell lines, GFP$^+$ [mCherry] cells were FACS-sorted 3 days after transfection to select for cells expressing the tagged nucleoporin. Individual clones were picked 6-7 days after sorting and characterized using immunofluorescence (to confirm the localization of the tagged protein at the nuclear periphery) and western blot (to identify clones lacking the endogenous protein). The selected clones were then further validated by PCR on genomic DNA and sequencing.

To achieve inducible degradation of GFP-mAID-Seh1, auxin (Sigma-Aldrich) was added to the medium at 500 µM (from a stock at 280 mM in ethanol). For control experiments, the same amount of ethanol was added.

Cell growth and differentiation assays

To evaluate cell growth at the pluripotent stage, cells were plated at $1\text{-}2\times10^5$ cells per well in a TPP 12-well plate. Photomicrographs were taken every 2 h using an IncuCyte live cell imager (Essen Biosciences, Ann Arbor, MI, USA) and confluence of the cultures was measured using IncuCyte software (Essen Biosciences, Ann Arbor, MI, USA). To improve comparisons between experiments or cell lines, the same mask was always used and time was set at t=0 when confluence reached 1% (Fig. 1D, Fig. 6C), 2% (Fig. 5C) or 3% (Fig. S1E). Graphs were generated using Excel. Data are mean±s.d. from the indicated (*n*) independent experiments.

Neuroectodermal differentiation of mESCs grown as monolayers was adapted from Ying and Smith (2003). Following trypsinization, feeders were removed by plating the resuspended cells in gelatin-free wells for 20 min. Feeder-free mESCs were collected and resuspended in N2B27 medium [DMEM F-12, DMEM Neurobasal, bovine serum albumin (BSA), L-glutamine, β-mercaptoethanol, N2 (Gibco) and B27 (Gibco)]. Cells were plated in gelatin-coated wells at 1×10^5 or 3×10^4 cells per well in a TPP 12-well plate. At day 2, N2B27 medium containing 1 µM retinoic acid (all-trans-retinoic acid, Sigma-Aldrich) was added for 24 h. From day 3 to 7, medium was changed every day with fresh N2B27 without retinoic acid. Confluence analyses, used as a proxy to evaluate cell growth and viability, was performed as described above, except that time was set at t=0, the beginning of the differentiation process (i.e. upon plating in N2B27 medium).

Fluorescence videomicroscopy

mESCs were transiently transfected using plasmids expressing H2B-GFP or H2B-mCherry on microscopy-adapted 35-mm dishes (µ-dish, 35 mm, high; Ibidi, Germany) coated with 0.1% gelatin and DR4-MEFs. Acquisitions were performed about 36 h after transfection at 37°C and 5% CO_2 using an AxioObserverZ1 inverted microscope (Zeiss, Germany) equipped with a 63 oil objective, a CSU-X1 spinning-disk head (Yokogawa, Japan) and a sCMOSPRIME 95B (Photometrics) camera.

The whole setup was driven with MetaMorph software (Molecular Devices, Sunnyvale, CA, USA). Eleven *z* sections with a step of 1 µm were acquired at 5 min intervals for the mitotic progression experiments (4-6 h) and at 15 min intervals for the cell cycle length experiments (24-30 h). Laser intensity was set between 10-20% power, and acquisition time was 500 ms. The raw data were processed using ImageJ software (National Institutes of Health, Bethesda, MD, USA). Images stacks were processed as maximum projections. Cells were tracked manually, setting prometaphase at the moment at which chromatin starts to be seen condensed, and anaphase at the first time point at which chromosome segregation is observed.

FACS analyses

To perform a bi-parametric analysis of cell cycle based on DNA content (DAPI) and DNA synthesis (EdU), we used Click-it-EdU Imaging kits (Invitrogen). mESCs (0.5×10^6) were plated on MEF-derived feeders plated on 0.1% gelatin 2 days before the experiment. Cells were incubated with EdU (50 µm) for 15 min, then collected by trypsinyzation and plated on gelatin dishes for 20 min to remove feeders.

Cells were then collected and centrifuged, washed in PBS and fixed in 3% paraformaldehyde for 15 min. Cells were then permeabilized with PBS plus 0.2% Triton X-100, and washed with PBS plus 2% FBS. Click reaction (30 min) was performed following the manufacturer's protocol. DNA was stained for 20 min (DAPI 5 µM, RNaseA 0.1 mg/ml, 1% FBS in PBS). Samples were then centrifuged and resuspended in 60 µl PBS plus 2% FBS.

Sample acquisition was achieved using an ImageStream X (Amnis, Austin, TX, USA) imaging flow cytometer and captured using the ISX INSPIRE data acquisition software. Images of 5000-20,000 cells were acquired at 40× magnification using the following channels: Ch1=430-470 nm, bright field; Ch6=720-800 nm, side scatter; Ch7=430-505 nm, DAPI; Ch9=570-595, bright field; Ch11=660-720 nm, EdU-AF647. A compensation matrix was generated using fluorescence controls and applied to all samples. Analysis was then performed with the IDEAS software as follows: (1) definition of cells in focus, based on the gradient RMS (root mean square for image sharpness); (2) definition of singlets, according to area and aspect ratio; (3) definition of cells using contrast and gradient RMS; (4) definition of nucleated cells using DNA content; (5) cell cycle phases were then identified using DAPI and EdU intensity; and (6) mitotic cells were finally defined according to DAPI bright detail intensity and DAPI area threshold (Fig. S2D).

Immunostaining and quantitative image analyses

mESCs grown on coverslips were washed with PBS, then fixed with 3% paraformaldehyde (VWR, Radnor, PA, USA) for 20 min and washed again with PBS. For all conditions, cells were then permeabilized in PBS plus 0.2% Triton X-100, 0.02% SDS (Euromedex, Souffelweyersheim, France) and 10 mg/ml BSA (Sigma-Aldrich). Antibody hybridizations and washes were also performed in this buffer. Primary and secondary antibodies (listed in Table S4) were incubated for 1 h at room temperature. Cells were then incubated for 5 min with 280 nM DAPI (Sigma-Aldrich) in PBS and mounted with Vectashield (Vector, Maravai Life Sciences, San Diego, CA, USA). Images were acquired using 100×/1.4 oil objectives on inverted and motorized microscopes, either a DMI8 (Leica) equipped with a CSU-W1 spinning-diskhead (Yokogawa, Japan) and 2 Orca-Flash 4 V2+ sCMOS cameras (Hamamatsu), or an Axio Observer.Z1 (Zeiss), equipped with CSU-X1 spinning-diskhead (Yokogawa, Japan) and 2 sCMOS PRIME 95 cameras (Photometrics).

Quantification of NPC density at the nuclear envelope was performed essentially as described previously (Souquet et al., 2018). Briefly, mESCs of interest were mixed with a GFP cell line of reference (*Rescue-Seh1* or *ΔE2-GFP-Nup85* cells, used for normalization) and grown on coverslips for 24 h before fixation and immunostaining. For each acquired image, one *z* section was selected; 8-pixel-thick regions of interest (ROI) were drawn

Journal of Cell Science (2021) 134, jcs258340. doi:10.1242/jcs.258340

freehand on the nuclear envelope of both GFP$^-$ and GFP$^+$ (reference) mESCs. Following subtraction of background, the signal intensity at the nuclear envelope for each cell was normalized to the average nuclear envelope intensity measured for the GFP$^+$ mESCs acquired in the same field. All values were then divided by the mean normalized intensity of wild-type mESCs acquired in the same experiment. Box plots were generated using GraphPad Software: each box encloses 50% of the normalized values obtained, centered on the median value. The bars extend from the fifth to 95th percentiles. Values falling outside of this range are displayed as individual points.

For kinetochore quantifications, mixed *GFP-Seh1* and Δ*E2-mCherry-Nup85/GFP-Seh1* mESCs grown on coverslips were fixed, permeabilized and stained with DAPI. Fields containing both *GFP-Seh1* and Δ*E2-mCherry-Nup85/GFP-Seh1* mitotic cells were selected. For each mitotic cell, the mean intensities of five distinct kinetochores (regions of ten pixels in diameter) and of two 'background' regions in the mitotic cytoplasm (40 pixels in diameter) were measured on a unique *z*-section. Following background subtraction, the average intensity of GFP-Seh1 at kinetochores in each mitotic cell was normalized to the intensity measured for the control (*wtNup85/ GFP-Seh1*) mitotic cells acquired in the same experiment. Box plots were generated as described above.

To quantify nuclear surfaces, mESCs of interest were mixed with a GFP cell line of reference and grown on coverslips for 24 h before fixation and immunostaining as described above. For each field, 33 to 45 optical sections (0.5 µm apart) were acquired and nuclei were segmented based on TPR immunostaining with the Fiji plug-in Lime-Seg (Machado et al., 2019). A circular ROI was drawn within the nucleus of each cell in the field and the LimeSeg plug-in 'Sphere Seg advanced' was run with the following parameters: D0, 4; Zscale, 7.143; range in D0 units, 2; real xy pixel size, 0.07; and F pressure, 0.025 for TPR-Cy3 staining and 0.019 for TPR-Cy5. Segmented structures for which the 'free edges' values were above 0 (segmentation could not close the structure), and those for which the Euler characteristic did not fall between −4/+4 (aberrant structures very far from a spherical shape) were discarded. For each cell, the segmentation perimeter and TPR staining along the *z*-axis were compared to further validate proper segmentation (less than 8% of the identified structures, frequently corresponding to the merge of two closely apposed nuclei, were manually discarded at that stage). Nuclear surfaces and volumes were then exported. To compensate for variability occurring during fixation or immunofluorescence processing, nuclear surface values were first normalized to the average of the GFP-reference cells acquired within the same coverslip, and then to the mean of wild-type mESCs acquired in the same experiment. Nuclear surface graphs were generated using GraphPad Software: average and s.d. (boxes and bars) of the nuclear surface are displayed, along with values for each experiment (dots).

Western blot analyses

To prepare whole cell lysates, mESCs were lysed in 2× Laemmli lysis buffer [150-mM Tris-HCL (pH 6.8), 5% (w/v) SDS, 25% (v/v) glycerol, and 0.01% (w/v) bromophenol blue]. Lysates were incubated for 3 min at 95°C, clarified by sonication (Bioruptordiagenode: 4 cycles of 30 s on/off, high power), and denatured again for 3 min at 95°C. Protein concentration was then determined using a BCA assay kit (Thermo Fisher Scientific). Total protein extracts supplemented with β-mercaptoethanol (750 mM final, Sigma-Aldrich) were analysed by western blot. mESC lysates (10 µg) were separated on 4-12% or 10% SDS-PAGE gels (pre-cast NuPage GE healthcare or Mini-Protean TGX Stain free precast gels, Biorad, Hercules, CA, USA) and transferred to nitrocellulose (GE Healthcare). The resulting blots were stained using Ponceau, saturated with TBS buffer plus 0.1% Tween 20 and 5% dried milk, and incubated in TBS plus 0.1% Tween 20 and 5% dried milk with primary antibodies, followed by either HRP-conjugated secondary antibodies of interest or HRP-conjugated anti-rabbit TrueBlot secondary antibody (used in Fig. 5B to prevent interference from the denatured/reduced heavy and light chains of the anti-Seh1 antibody used for immunoprecipitation) (primary and secondary antibodies are listed in Table S4). Signals were detected by enhanced chemiluminescence (SuperSignal Pico or Femto, Thermo Fisher Scientific) using ChemiDoc (Bio-Rad).

Immunoprecipitation experiments and mass spectrometry analyses

For immunoprecipitation experiments, Protein G beads (GE Healthcare) were washed three times with wash buffer [100 mM NaCl, 1 mM EDTA, 25 mM Tris (pH 7.5), 1 mM DTT plus protease inhibitor (Pi) solution]. Bead centrifugations were performed at 500 ***g*** at 4°C. Beads (30 µl) were then incubated for 2 h at 4°C in 250 µl wash buffer containing 5 µl of rabbit anti-Seh1 antibody (for Fig. 5B), or 25 µl of rabbit polyclonal anti-Nup107 or anti-Nup85 serum or a pre-immune rabbit serum as control (for Fig. S3B). After incubation, the beads were washed four times with wash buffer.

In the meantime, lysates were prepared from wild-type, *Seh1*$^{-/-}$, *Mios*$^{-/-}$ or Δ*E2-GFP-Nup85* mESCs by resuspending frozen pellets of 4×10^6 mESCs (~500 µg total proteins) in 200 µl lysis buffer [100 mM NaCl, 1 mM EDTA, 25 mM Tris (pH 7.5), 1 mM DTT, 0.5% Tween 20, 1.2% Triton X-100 plus Pi solution]. Samples were vortexed and incubated for 15 min on ice. An aliquot of 600 µl of dilution buffer [100 mM NaCl, 1 mM EDTA, 25 mM Tris (pH 7.5), 1 mM DTT, 0.5% Tween 20 plus Pi solution] was then added and samples were centrifuged at 16,000 ***g*** for 30 min at 4°C. The resulting supernatants were pre-cleared by a 1 h incubation at 4°C with 30 µl Protein G beads equilibrated with wash buffer.

The cleared supernatants (inputs) were then incubated at 4°C with 30 µl of the anti-Seh1-, control-, anti-Nup107- or anti-Nup85-coated Protein G beads. After overnight (for anti-Seh1) or 2 h incubation (for anti-Nup107 and anti-Nup85), samples were centrifuged and washed five times in wash buffer. The proteins were either eluted in 40 µl of Laemmli and boiled 10 min for subsequent western blot analysis (Fig. 5B), or split in two and then either eluted in 20 µl of Laemmli and boiled 3 min for subsequent western blot analyses, or processed for mass spectrometry (MS) analyses (for experiments presented in Fig. S3).

For sample preparation before liquid chromatography (LC)-MS/MS analysis, proteins on beads were digested overnight at 37°C with trypsin (Promega, Madison, WI, USA) in a 25-mM NH_4HCO_3 buffer (0.2 µg trypsin in 20 µl). The resulting peptides were desalted using ZipTip µ-C18 Pipette Tips (Pierce Biotechnology, Rockford, IL, USA).

LC-MS/MS acquisition

Samples were analyzed using an Orbitrap Fusion coupled to a Nano-LC Proxeon 1200 equipped with an easy spray ion source (Thermo Fisher Scientific, Waltham, MA, USA). Peptides were loaded with an online pre-concentration method and separated by chromatography using a Pepmap-RSLC C18 column (0.75×750 mm, 2 µm, 100 Å) from Thermo Fisher Scientific, equilibrated at 50°C and operated at a flow rate of 300 nl/min. Solvents [MS grade H_2O, formic acid (FA) and Acetonitrile (ACN)] were obtained from Thermo Chemical (Waltham, MA, USA).

Peptides were eluted by a gradient of solvent A (H_2O, 0.1% FA) and solvent B (ACN/H_2O 80/20, 0.1% FA). The column was first equilibrated for 5 min with 95% of solvent A, then solvent B was raised to 28% in 105 min and to 40% in 15 min. Finally, the column was washed with 95% solvent B for 20 min and re-equilibrated with 95% solvent A for 10 min. On the Orbitrap Fusion instrument, peptide precursor masses were analyzed in the Orbitrap cell in full ion scan mode at a resolution of 120,000, a mass range of *m/z* 350-1550 and an AGC target of 4×10^5. MS/MS was performed using the top speed 3 s mode. Peptides were selected for fragmentation by higher-energy C-trap dissociation with a normalized collisional energy of 27% and a dynamic exclusion of 60 s. Fragment masses were measured in an ion trap in the rapid mode, with an AGC target of 1×10^4. Monocharged peptides and unassigned charge states were excluded from the MS/MS acquisition. The maximum ion accumulation times were set to 100 ms for MS and 35 ms for MS/MS acquisitions.

For data analysis, raw data were processed on Proteome Discoverer 2.2 with the mascot node (Mascot version 2.5.1) and the Swissprot protein database release 2017_06. The *Mus musculus* taxonomy was used and a maximum of two missed cleavages was authorized. Precursor and fragment mass tolerances were set to 7 ppm and 0.5 Da. The following post-translational modifications were included as variable: acetyl (Protein N-term), oxidation (M), phosphorylation (STY). Spectra were filtered using a 1% false discovery rate with the percolator node.

Statistics

For cell confluence analyses, statistical analyses were performed at the latest time points (48 h for cell growth in the pluripotent state and day 5 for neuroectodermal differentiation) using a paired two-tailed Student's *t*-test. For each mutant cell line, the percentage of confluence was compared to that of wild-type cells measured in the same experiment. To obtain more robust statistics, the paired two-tailed Student's *t*-test was also used to compare all the values obtained with distinct clones bearing the same mutation to wild-type cells. For studies of interphase and mitosis duration and for quantifications of fluorescence intensity at the nuclear envelope, statistical analyses were performed using an unpaired non-parametric Mann–Whitney test. For nuclear surfaces, statistical analyses were performed using a paired two-tailed Student's *t*-test. ****P<0.0001, ***P<0.001, **P<0.01 and *P<0.05.

Acknowledgements

We thank V. Heyer for generating the CRISPR/Cas9 vectors; B. Souquet and A. Berto for advice regarding mESC culture; P. Navarro and N. Festuccia for advice and reagents regarding integration at the *Tigre* locus and degron approaches; Jan Kosinski for discussions about the Nup85-Seh1 model; D. Forbes for sharing the Nup85 antibodies; N. Minc and S. Dmitrieff for their advice regarding the analysis of nuclear size; Liang Zhang for advice regarding anti-Seh1 immunoprecipitation experiments; and C. Boumendil and R. Karess for critical reading of the manuscript. We also thank the proteomics core facility at the Institut Jacques-Monod, notably C. Garcia and L. Lignières, for the LC-MS/MS experiments. We also acknowledge the ImagoSeine core facility of the Institut Jacques Monod, notably M. Fradet and X. Baudin for help with cell sorting and spinning disk imaging, respectively.

Competing interests

The authors declare no competing or financial interests.

Author contributions

Conceptualization: A.G.-E., A.V., B.R.-S.-M., V.D.; Methodology: A.G.-E., A.V., C.O., B.R.-S.-M., V.D.; Validation: A.G.-E, A.V., V.D.; Formal analysis: A.G.-E., A.V., C.O., V.D.; Investigation: A.G.-E., A.V., C.O., V.D.; Data curation: A.G.-E., A.V., V.D.; Writing - original draft: A.G.-E., A.V., V.D.; Writing - review & editing: A.G.-E., A.V., C.O., V.D.; Visualization: A.G.-E., A.V., V.D.; Supervision: V.D.; Funding acquisition: V.D.

Funding

Work in the laboratory of V.D. was supported by the Centre National de la Recherche Scientifique (CNRS), the 'Fondation pour la Recherche Médicale' (Foundation for Medical Research) (DEQ20150734355, 'Equipe FRM 2015' to V.D.) and by the Labex Who Am I? (ANR-11-LABX-007 and Idex ANR-11-IDEX-0005-02). A.G.-E. received a PhD fellowship from the Marie Skłodowska-Curie actions co-funding of regional, national and international programmes (INSPIRE, H2020-MSCA-COFUND-2014 No 665850) and a transition post-doc grant from Labex Who Am I?, A.V. received a post-doc grant from Labex Who Am I? and C.O. received a fellowship from Ecole Doctorale BioSPC, Université de Paris. Part of the LC-MS/MS equipment was funded by the Region Ile-de-France (SESAME 2013 Q-Prot-B&M - LS093471), Université Paris Diderot (ARS 2014-2018) and the CNRS (Moyens d'Equipement Exceptionnel INSB 2015). The ImagoSeine core facility was supported by funds from IBISA (Infrastructures en Biologie Santé et Agronomie) and the France-Bioimaging (ANR-10-INBS-04) infrastructures.

Data availability

The MS proteomics data reported in this study have been deposited in the ProteomeXchange Consortium database via the PRIDE partner repository (Perez-Riverol et al., 2019), with the dataset identifier PXD022190. The original 16-bit images and montages of the western blots used in this study are available as a Mendeley dataset available from http://www.dx.doi.org/10.17632/8g59mp92bs.2.

Peer review history

The peer review history is available at https://journals.biologists.com/jcs/article-lookup/doi/10.1242/jcs.258340

References

Algret, R., Fernandez-Martinez, J., Shi, Y., Kim, S. J., Pellarin, R., Cimermancic, P., Cochet, E., Sali, A., Chait, B. T., Rout, M. P. et al. (2014). Molecular architecture and function of the SEA complex, a modulator of the TORC1 pathway. *Mol. Cell. Proteomics* **13**, 2855-2870. doi:10.1074/mcp.M114.039388

Bar-Peled, L., Chantranupong, L., Cherniack, A. D., Chen, W. W., Ottina, K. A., Grabiner, B. C., Spear, E. D., Carter, S. L., Meyerson, M. and Sabatini, D. M. (2013). A Tumor suppressor complex with GAP activity for the Rag GTPases that signal amino acid sufficiency to mTORC1. *Science* **340**, 1100-1106. doi:10.1126/science.1232044

Brohawn, S. G., Leksa, N. C., Spear, E. D., Rajashankar, K. R. and Schwartz, T. U. (2008). Structural evidence for common ancestry of the nuclear pore complex and vesicle coats. *Science* **322**, 1369-1373. doi:10.1126/science.1165886

Buchwalter, A., Kaneshiro, J. M. and Hetzer, M. W. (2019). Coaching from the sidelines: the nuclear periphery in genome regulation. *Nat. Rev. Genet.* **20**, 39-50. doi:10.1038/s41576-018-0063-5

Cai, W., Wei, Y., Jarnik, M., Reich, J. and Lilly, M. A. (2016). The GATOR2 component Wdr24 regulates TORC1 activity and lysosome function. *PLoS Genet.* **12**, e1006036. doi:10.1371/journal.pgen.1006036

Debler, E. W., Ma, Y., Seo, H. S., Hsia, K. C., Noriega, T. R., Blobel, G. and Hoelz, A. (2008). A fence-like coat for the nuclear pore membrane. *Mol. Cell* **32**, 815-826. doi:10.1016/j.molcel.2008.12.001

Dokudovskaya, S. and Rout, M. P. (2015). SEA you later alli-GATOR - a dynamic regulator of the TORC1 stress response pathway. *J. Cell Sci.* **128**, 2219-2228. doi:10.1242/jcs.168922

Doucet, C. M., Talamas, J. A. and Hetzer, M. W. (2010). Cell cycle-dependent differences in nuclear pore complex assembly in metazoa. *Cell* **141**, 1030-1041. doi:10.1016/j.cell.2010.04.036

Engler, C., Gruetzner, R., Kandzia, R. and Marillonnet, S. (2009). Golden gate shuffling: a one-pot DNA shuffling method based on type IIs restriction enzymes. *PLoS ONE* **4**, e5553. doi:10.1371/journal.pone.0005553

Faria, A. M. C., Levay, A., Wang, Y., Kamphorst, A. O., Rosa, M. L. P., Nussenzveig, D. R., Balkan, W., Chook, Y. M., Levy, D. E. and Fontoura, B. M. A. (2006). The nucleoporin Nup96 is required for proper expression of interferon-regulated proteins and functions. *Immunity* **24**, 295-304. doi:10.1016/j.immuni.2006.01.014

Fernandez-Martinez, J., Kim, S. J., Shi, Y., Upla, P., Pellarin, R., Gagnon, M., Chemmama, I. E., Wang, J., Nudelman, I., Zhang, W. et al. (2016). Structure and function of the nuclear pore complex cytoplasmic mRNA export platform. *Cell* **167**, 1215-1228.e25. doi:10.1016/j.cell.2016.10.028

Hampoelz, B., Andres-Pons, A., Kastritis, P. and Beck, M. (2019). Structure and assembly of the nuclear pore complex. *Annu. Rev. Biophys.* **48**, 515-536. doi:10.1146/annurev-biophys-052118-115308

Harel, A., Orjalo, A. V., Vincent, T., Lachish-Zalait, A., Vasu, S., Shah, S., Zimmerman, E., Elbaum, M. and Forbes, D. J. (2003). Removal of a single pore subcomplex results in vertebrate nuclei devoid of nuclear pores. *Mol. Cell* **11**, 853-864. doi:10.1016/S1097-2765(03)00116-3

Hezwani, M. and Fahrenkrog, B. (2017). The functional versatility of the nuclear pore complex proteins. *Semin. Cell Dev. Biol.* **68**, 2-9. doi:10.1016/j.semcdb.2017.05.004

Huang, G., Zhang, Y., Zhu, X., Zeng, C., Wang, Q., Zhou, Q., Tao, Q., Liu, M., Lei, J., Yan, C.et al. (2020). Structure of the cytoplasmic ring of the Xenopus laevis nuclear pore complex by cryo-electron microscopy single particle analysis. *Cell Res.* **30**, 520-531. doi:10.1038/s41422-020-0319-4

Jevtić, P., Mukherjee, R. N., Chen, P. and Levy, D. L. (2019). Altering the levels of nuclear import factors in early Xenopus laevis embryos affects later development. *PLoS ONE* **14**, e0215740. doi:10.1371/journal.pone.0215740

Kosinski, J., Mosalaganti, S., von Appen, A., Teimer, R., DiGuilio, A. L., Wan, W., Bui, K. H., Hagen, W. J. H., Briggs, J. A. G., Glavy, J. S. et al. (2016). Molecular architecture of the inner ring scaffold of the human nuclear pore complex. *Science* **352**, 363-365. doi:10.1126/science.aaf0643

Lin, D. H. and Hoelz, A. (2019). The structure of the nuclear pore complex (An Update). *Annu. Rev. Biochem.* **88**, 725-783. doi:10.1146/annurev-biochem-062917-011901

Liu, Z., Yan, M., Liang, Y., Liu, M., Zhang, K., Shao, D., Jiang, R., Li, L., Wang, C., Nussenzveig, D. R. et al. (2019). Nucleoporin Seh1 interacts with Olig2/Brd7 to promote oligodendrocyte differentiation and myelination. *Neuron* **102**, 587-601.e7. doi:10.1016/j.neuron.2019.02.018

Loiodice, I., Alves, A., Rabut, G., Van Overbeek, M., Ellenberg, J., Sibarita, J. B. and Doye, V. (2004). The entire Nup107-160 complex, including three new members, is targeted as one entity to kinetochores in mitosis. *Mol. Biol. Cell* **15**, 3333-3344. doi:10.1091/mbc.e03-12-0878

Lupu, F., Alves, A., Anderson, K., Doye, V. and Lacy, E. (2008). Nuclear pore composition regulates neural stem/progenitor cell differentiation in the mouse embryo. *Dev. Cell* **14**, 831-842. doi:10.1016/j.devcel.2008.03.011

Machado, S., Mercier, V. and Chiaruttini, N. (2019). LimeSeg: a coarse-grained lipid membrane simulation for 3D image segmentation. *BMC Bioinformatics* **20**, 2. doi:10.1186/s12859-018-2471-0

Moreira, T. G., Zhang, L., Shaulov, L., Harel, A., Kuss, S. K., Williams, J., Shelton, J., Somatilaka, B., Seemann, J., Yang, J. et al. (2015). Sec13 regulates expression of specific immune factors involved in inflammation in vivo. *Sci. Rep.* **5**, 17655. doi:10.1038/srep17655

Natsume, T., Kiyomitsu, T., Saga, Y. and Kanemaki, M. T. (2016). Rapid protein depletion in human cells by auxin-inducible degron tagging with short homology donors. *Cell Rep.* **15**, 210-218. doi:10.1016/j.celrep.2016.03.001

Neumann, N., Lundin, D. and Poole, A. M. (2010). Comparative genomic evidence for a complete nuclear pore complex in the last eukaryotic common ancestor. *PLoS ONE* **5**, e13241. doi:10.1371/journal.pone.0013241

Okita, K., Kiyonari, H., Nobuhisa, I., Kimura, N., Aizawa, S. and Taga, T. (2004). Targeted disruption of the mouse ELYS gene results in embryonic death at peri-implantation development. *Genes Cells* **9**, 1083-1091. doi:10.1111/j.1365-2443.2004.00791.x

Pascual-Garcia, P. and Capelson, M. (2019). Nuclear pores in genome architecture and enhancer function. *Curr. Opin. Cell Biol.* **58**, 126-133. doi:10.1016/j.ceb.2019.04.001

Perez-Riverol, Y., Csordas, A., Bai, J., Bernal-Llinares, M., Hewapathirana, S., Kundu, D. J., Inuganti, A., Griss, J., Mayer, G., Eisenacher, M. et al. (2019). The PRIDE database and related tools and resources in 2019: improving support for quantification data. *Nucleic Acids Res.* **47**, D442-D450. doi:10.1093/nar/gky1106

Platani, M., Santarella-Mellwig, R., Posch, M., Walczak, R., Swedlow, J. R. and Mattaj, I. W. (2009). The Nup107-160 nucleoporin complex promotes mitotic events via control of the localization state of the chromosome passenger complex. *Mol. Biol. Cell* **20**, 5260-5275. doi:10.1091/mbc.e09-05-0377

Platani, M., Trinkle-Mulcahy, L., Porter, M., Jeyaprakash, A. A. and Earnshaw, W. C. (2015). Mio depletion links mTOR regulation to Aurora A and Plk1 activation at mitotic centrosomes. *J. Cell Biol.* **210**, 45-62. doi:10.1083/jcb.201410001

Platani, M., Samejima, I., Samejima, K., Kanemaki, M. T. and Earnshaw, W. C. (2018). Seh1 targets GATOR2 and Nup153 to mitotic chromosomes. *J. Cell Sci.* **131**, jcs213140. doi:10.1242/jcs.213140

Rabut, G., Doye, V. and Ellenberg, J. (2004). Mapping the dynamic organization of the nuclear pore complex inside single living cells. *Nat. Cell Biol.* **6**, 1114-1121. doi:10.1038/ncb1184

Rasala, B. A., Orjalo, A. V., Shen, Z. X., Briggs, S. and Forbes, D. J. (2006). ELYS is a dual nucleoporin/kinetochore protein required for nuclear pore assembly and proper cell division. *Proc. Natl. Acad. Sci. USA* **103**, 17801-17806. doi:10.1073/pnas.0608484103

Salama, N. R., Yeung, T. and Schekman, R. W. (1993). The Sec13p complex and reconstitution of vesicle budding from the Er with purified cytosolic proteins. *EMBO J.* **12**, 4073-4082. doi:10.1002/j.1460-2075.1993.tb06091.x

Scholz, B. A., Sumida, N., de Lima, C. D. M., Chachoua, I., Martino, M., Tzelepis, I., Nikoshkov, A., Zhao, H. L., Mehmood, R., Sifakis, E. G. et al. (2019). WNT signaling and AHCTF1 promote oncogenic MYC expression through super-enhancer-mediated gene gating. *Nat. Genet.* **51**, 1723-1731. doi:10.1038/s41588-019-0535-3

Selfridge, J., Pow, A. M., McWhir, J., Magin, T. M. and Melton, D. W. (1992). Gene targeting using a mouse HPRT minigene/HPRT-deficient embryonic stem cell system: Inactivation of the mouseERCC-1 gene. *Somat Cell Mol. Genet***18**, 325-336. doi:10.1007/BF01235756

Senger, S., Csokmay, J., Tanveer, A., Jones, T. I., Sengupta, P. and Lilly, M. A. (2011). The nucleoporin Seh1 forms a complex with Mio and serves an essential tissue-specific function in Drosophila oogenesis. *Development* **138**, 2133-2142. doi:10.1242/dev.057372

Souquet, B., Freed, E., Berto, A., Andric, V., Auduge, N., Reina-San-Martin, B., Lacy, E. and Doye, V. (2018). Nup133 is required for proper nuclear pore basket assembly and dynamics in embryonic stem cells. *Cell Rep.* **23**, 2443-2454. doi:10.1016/j.celrep.2018.04.070

Terashima, Y., Toda, E., Itakura, M., Otsuji, M., Yoshinaga, S., Okumura, K., Shand, F. H. W., Komohara, Y., Takeda, M., Kokubo, K. et al. (2020). Targeting FROUNT with disulfiram suppresses macrophage accumulation and its tumor-promoting properties. *Nat. Commun.* **11**, 609. doi:10.1038/s41467-020-14338-5

Vollmer, B., Lorenz, M., Moreno-Andrés, D., Bodenhöfer, M., De Magistris, P., Astrinidis, S. A., Schooley, A., Flötenmeyer, M., Leptihn, S. and Antonin, W. (2015). Nup153 recruits the Nup107-160 complex to the inner nuclear membrane for interphasic nuclear pore complex assembly. *Dev. Cell* **33**, 717-728. doi:10.1016/j.devcel.2015.04.027

von Appen, A., Kosinski, J., Sparks, L., Ori, A., DiGuilio, A. L., Vollmer, B., Mackmull, M. T., Banterle, N., Parca, L., Kastritis, P. et al. (2015). In situ structural analysis of the human nuclear pore complex. *Nature* **526**, 140-143. doi:10.1038/nature15381

Walther, T. C., Alves, A., Pickersgill, H., Loiodice, I., Hetzer, M., Galy, V., Hulsmann, B. B., Kocher, T., Wilm, M., Allen, T. et al. (2003). The conserved Nup107-160 complex is critical for nuclear pore complex assembly. *Cell* **113**, 195-206. doi:10.1016/S0092-8674(03)00235-6

Webster, B. M. and Lusk, C. P. (2016). Border safety: quality control at the nuclear envelope. *Trends Cell Biol.* **26**, 29-39. doi:10.1016/j.tcb.2015.08.002

Ying, Q. L. and Smith, A. G. (2003). Defined conditions for neural commitment and differentiation. *Methods Enzymol.* **365**, 327-341. doi:10.1016/S0076-6879(03)65023-8

Zeng, H., Horie, K., Madisen, L., Pavlova, M. N., Gragerova, G., Rohde, A. D., Schimpf, B. A., Liang, Y., Ojala, E., Kramer, F. et al. (2008). An inducible and reversible mouse genetic rescue system. *PLoS Genet.* **4**, e1000069. doi:10.1371/journal.pgen.1000069

Zuccolo, M., Alves, A., Galy, V., Bolhy, S., Formstecher, E., Racine, V., Sibarita, J. B., Fukagawa, T., Shiekhattar, R., Yen, T. et al. (2007). The human Nup107-160 nuclear pore subcomplex contributes to proper kinetochore functions. *EMBO J.* **26**, 1853-1864. doi:10.1038/sj.emboj.7601642